QCD deconfinement transition line up to $\mu_B = 400$ MeV from finite volume lattice simulations

Szabolcs Borsányi,[1] Zoltán Fodor,[1,2,3,4] Jana N. Guenther,[1] Paolo Parotto,[5] Attila Pásztor,[3] Ludovica Pirelli,[1] Kálmán K. Szabó,[1,4] and Chik Him Wong[1]

[1]*Department of Physics, Wuppertal University, Gaußstraße 20, D-42119, Wuppertal, Germany*
[2]*Pennsylvania State University, Department of Physics, State College, Pennsylvania 16801, USA*
[3]*Institute for Theoretical Physics, ELTE Eötvös Loránd University, Pázmány P. sétány 1/A, H-1117 Budapest, Hungary*
[4]*Jülich Supercomputing Centre, Forschungszentrum Jülich, D-52425 Jülich, Germany*
[5]*Dipartimento di Fisica, Università di Torino and INFN Torino, Via P. Giuria 1, I-10125 Torino, Italy*

(Received 22 October 2024; accepted 25 November 2024; published 30 December 2024)

The QCD crossover line in the temperature (T)-baryochemical potential (μ_B) plane has been computed by several lattice groups by calculating the chiral order parameter and its susceptibility at finite values of μ_B. In this work we focus on the deconfinement aspect of the transition between hadronic and quark gluon plasma phases. We define the deconfinement temperature as the peak position of the static quark entropy $[S_Q(T,\mu_B)]$ in T, which is based on the renormalized Polyakov loop. We extrapolate $S_Q(T,\mu_B)$ based on high statistics finite temperature ensembles on a $16^3 \times 8$ lattice to finite density by means of a Taylor expansion to eighth order in μ_B (NNNLO) along the strangeness neutral line. For the simulations the 4HEX staggered action was used with $2+1$ flavors at physical quark masses. In this setup the phase diagram can be drawn up to unprecedentedly high chemical potentials. Our results for the deconfinement temperature are in rough agreement with phenomenological estimates of the freeze-out curve in relativistic heavy ion collisions. In addition, we study the width of the deconfinement crossover. We show that up to $\mu_B \approx 400$ MeV, the deconfinement transition gets broader at higher densities, disfavoring the existence of a deconfinement critical endpoint in this range. Finally, we examine the transition line without the strangeness neutrality condition and observe a hint for the narrowing of the crossover towards large μ_B.

DOI: 10.1103/PhysRevD.110.114507

I. INTRODUCTION

In the last decades, a large body of evidence has been gathered on the crossover transition between the hadronic and quark gluon plasma (QGP) phases of QCD at zero net baryon density, both from theory [1–6] and the phenomenology of heavy ion collision experiments [7–9]. Theoretically, there are two distinct aspects of the QCD transition. One is chiral symmetry restoration and the other is deconfinement.

Chiral symmetry restoration is defined in the limit of zero light quark masses (the chiral limit), when chiral symmetry becomes exact. In this limit, it is generally expected that a genuine phase transition will take place, instead of a crossover, with the order of the transition depending on the number of quark flavors [6,10–12]. The most relevant for phenomenology is the two-flavor chiral limit, where a second order transition in the $O(4)$ universality class is expected. Chiral symmetry restoration is studied mostly through the mass derivatives of the free energy: the chiral condensate and the (full or disconnected) chiral susceptibilities. Lattice studies have determined the crossover temperature in the case of physical quark masses by locating the peak of these susceptibilities [2,4,13,14]. The behavior of these observables closer to the chiral limit was also studied on the lattice [15–17].

Deconfinement, on the other hand, is most cleanly defined in the limit of infinite quark masses, where center symmetry becomes exact. In this quenched limit there is a weak first order transition between the confined and deconfined gluon plasma phases (for a recent high precision study, see Ref. [18]).

An approximate order parameter for the deconfinement transition is the Polyakov loop, which probes the properties of infinite mass static test quarks in a QCD medium [19]. Its use is not limited to infinite quark masses: it has proven useful to study the nature of the transition with heavy quarks [20], even down to physical masses [13,21–23].

It was also studied for smaller-than-physical quark masses, where it was observed that a rapid rise of the Polyakov loop still accompanies the chiral transition [24].

Several observables can be derived from the Polyakov loop to study confinement. A good review of these is Ref. [25], where it is demonstrated that the static quark entropy has some favorable properties to study deconfinement numerically on the lattice. Furthermore, it also has a peak position that is very close to the value of the chiral crossover temperature.

While the crossover nature of the transition is very well established at zero baryon density (or baryochemical potential μ_B), it is predicted by model and functional calculations that the transition line in the T-μ_B plane turns into a first order transition at higher baryon densities at a critical endpoint [26–32]. The experimental discovery of the QCD critical endpoint is a major goal of relativistic heavy ion collision experiments [33].

However, at this point in time very little is known for certain about the QCD phase diagram. One example is the curvature of the crossover temperature in μ_B. Defined via observables related to chiral symmetry restoration, it is currently very well established [17,34–36]. The chiral transition line $T_c(\mu_B)$ was also studied using multipoint Padé approximants in Ref. [37].

On the other hand, observables related to deconfinement have been studied much less at nonzero chemical potential. The first study to compute the leading Taylor coefficient of the static quark free energy in μ_B^2 was Ref. [38], where it was noted that this coefficient develops a peak near the chiral crossover temperature. In Ref. [39] the chiral crossover temperature was compared to the deconfinement temperature, defined as the peak position of the static quark entropy. The volume dependence of both aspects were studied including their leading μ_B^2 dependence. It was found that chiral and deconfinement related observables have different behaviors. First, deconfinement properties have a milder volume dependence. Second, the curvature of the crossover line is slightly larger for the deconfinement transition. Finally, the deconfinement transition appears to get broader with increasing μ_B (at least up to leading order in μ_B), while the width as well as the strength of the chiral transition are approximately constant.

The main goal of this work is to further study the deconfinement properties of the QCD medium at nonzero μ_B, by extending the accessible range in baryochemical potential. By calculating the Taylor coefficients of the static quark free energy to order μ_B^8 and expanding around zero, we cover a range up to $\mu_B \approx 400$ MeV.

We simulate lattices with a fixed number of time slices, $N_t = 8$. However, we expect cutoff effects to be very small. This expectation is based on our previous work with the same discretization [40], where we showed that the value of the fluctuations of the baryon number (up to eighth order) for this discretization is very close to the continuum limit.

In order to achieve a good signal for the μ_B^8 coefficient, we carry out our study in a smaller 3-volume $LT = 2$. We showed in Ref. [39] that quantities related to the Polyakov loop have much milder finite volume effects than chiral observables. The crossover temperature in the volume we simulate is about 10 MeV higher than its infinite volume value. Compared to the infinite volume chiral transition temperature, it is only 5 MeV higher. We thus expect the finite volume effects in our study to be small, though not completely negligible.

An important technical aspect of drawing phase diagrams in the T-μ_B plane is how one handles strangeness. In this paper, we study both the phenomenologically more relevant case of zero strangeness expectation value ($n_S = 0$, strangeness neutrality) as well as the technically easier case of zero strangeness chemical potential ($\mu_S = 0$).

Our final results are the deconfinement transition temperature and the width of the deconfinement transition as a function of the chemical potential. For the strangeness neutral case they are shown in Fig. 1. On the left, the deconfinement crossover temperature calculated in this work is compared to the chiral crossover temperature from Ref. [34] and an estimate of the freeze-out parameters in heavy ion collisions by the STAR Collaboration [41] and the parametrization in Ref. [42]. On the right we show the chiral transition width from Ref. [34] and the deconfinement width from this work. Already at $\mu_B = 0$ the deconfinement transition is much broader. Even more interestingly, as a function of the baryochemical potential, the deconfinement transition broadens, while the width of the chiral transition stays roughly the same. This contrasting behavior was already observed in our earlier work [39], but only to leading order in μ_B. Here, we observe the same behavior in a large range of chemical potential. Our results disfavor the existence of a deconfinement critical endpoint below $\mu_B \approx 400$ MeV. As will be shown in Sec. III C, the same statement is also true for zero strangeness chemical potential. However, in that setup, we see the reverse trend of the width. Above $\mu_B \approx 300$ MeV the width of the deconfinement transition gets smaller again. This is what one expects if a critical endpoint exists somewhere above $\mu_B = 400$ MeV.

The paper is organized as follows. In Sec. II we motivate our choice of observable to define the deconfinement temperature. We work out the details of its extrapolation to finite density through a Taylor expansion in μ_B/T, and describe the renormalization procedure. Cross-checking with ensembles at imaginary μ_B, we validate the results extrapolated with the Taylor expansion. Note that the extrapolation itself uses solely $\mu_B = 0$ ensembles. In Sec. III we use the extrapolated static quark free energy to determine the deconfinement temperature up to $\mu_B = 400$ MeV and characterize the strength of the transition. We also compare the cases with and without imposing strangeness neutrality. Finally, we summarize our conclusions in Sec. IV.

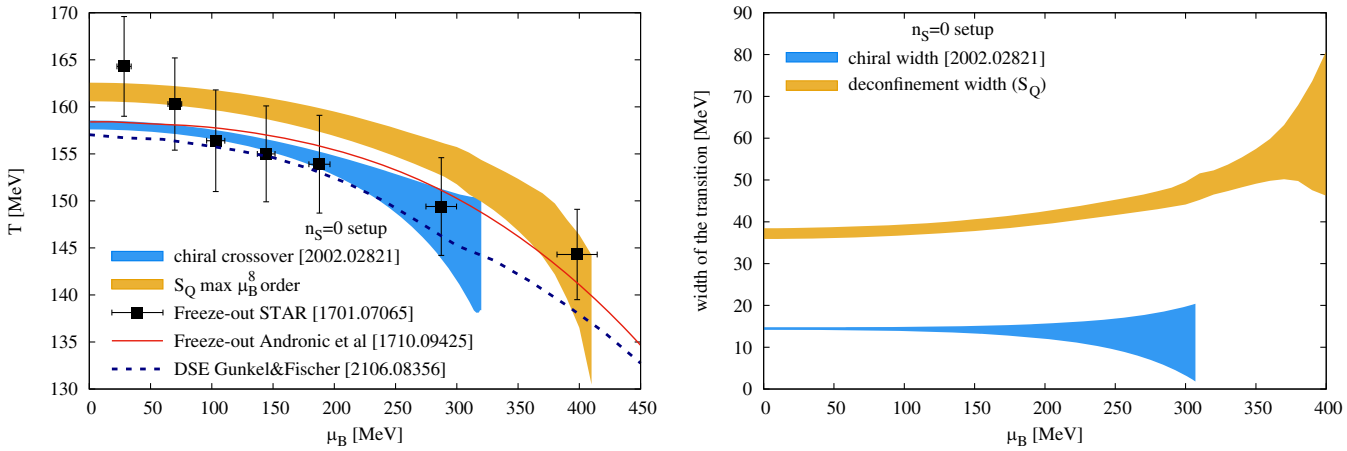

FIG. 1. Left: the deconfinement line (orange) defined as the peak position of the static quark entropy (S_Q) at fixed μ_B as a function of μ_B. We add the chiral transition line from lattice QCD [34] in the phase diagram, defined from the peak of the full chiral susceptibility, as well as the corresponding result based on Dyson-Schwinger equations [26] (the latter used the $\mu_S = \mu_B/3$ scheme as an approximation to $n_S = 0$). We also include the chemical freeze-out parameters [41,42]. Right: the width associated to the deconfinement (orange) and chiral (blue) transitions: the two differ already at $\mu_B = 0$. With increasing μ_B, while the chiral width is mostly constant, the deconfinement width grows.

II. STATIC QUARK FREE ENERGY AT FINITE DENSITY

The main observable calculated in this work is the static quark free energy F_Q, that is based on the expectation value P of the Polyakov loop:

$$P = \frac{1}{3}\frac{1}{V}\left\langle \sum_{\vec{x}\in V} \mathrm{Tr} \prod_{t=0}^{N_t-1} U_0(t,\vec{x}) \right\rangle. \tag{1}$$

Here the product refers to the multiplication of the temporal link variables (U_t) of the gauge field along the entire temporal direction of the lattice that consists of N_t time slices. Thus, a Wilson line is formed and its normalized trace is the Polyakov loop. It is averaged over the three-volume V as well as over the ensemble of gauge configurations.

From P, the static quark free energy is then defined as

$$F_Q = -T \log P. \tag{2}$$

The Polyakov loop has been a popular observable to study deconfinement for a long time. This is especially true in the quenched approximation where the deconfinement transition is characterized by the spontaneous symmetry breaking of the center symmetry of the gauge group. The Polyakov loop acts as an order parameter for this symmetry breaking transition, and its susceptibility χ diverges with the volume at the transition temperature. In full QCD the role of the Polyakov loop is less evident, especially in the theory with physical masses, where chiral features are dominant. Yet, it was observed that the Polyakov loop exhibits a significant rise near the chiral transition temperature. With physical quark masses, the deconfinement transition is a very broad crossover and the Polyakov loop susceptibility does not provide a clean signature for the transition.

In dynamical QCD the main difficulty with the Polyakov loop is its scheme dependence. It requires a multiplicative renormalization that is fixed through an ambiguous procedure. Luckily, the scheme dependence reduces to an additive term in $F_Q(T,\mu_B)$ that depends on the lattice cutoff, but not on the infrared control parameters, such as T and μ_B. We work on the details of renormalization in Sec. II D.

It follows from the additive nature of the F_Q renormalization that the static quark entropy,

$$S_Q(T,\mu_B) = -\frac{\partial F_Q(T,\mu_B)}{\partial T}, \tag{3}$$

is well defined, and the scheme dependence cancels in the continuum limit. It was shown that the crossover temperature defined via $S_Q(T)$ approximately coincides with the chiral transition temperature for various nonzero values of the quark mass, including the physical case [25]. In the chiral limit $S_Q(T)$ was shown to exhibit a spike at the chiral T_c [24]. In contrast, the susceptibility of the Polyakov loop could not be used to locate the transition because of its strong scheme dependence.

In a recent work [39] we determined the peak position of S_Q for several values of imaginary chemical potential and found that it follows the chiral transition. For large volumes, we found that the peak in $S_Q(T)$ is at a temperature roughly 5 MeV lower than the disconnected chiral susceptibility, but its volume dependence was considerably

smaller compared to any of the chiral observables. This was expected, since $S_Q(T)$ probes QCD with static (infinite mass) quarks, while chiral quantities access the theory at the pion mass scale. By reducing the volume from the near-infinite choice of $LT = 4$, frequently found in the literature, we are able to compute S_Q at higher density by using an eighth order Taylor extrapolation.

In the following we work out the Taylor extrapolation coefficients of the Polyakov loop and construct the extrapolation of the static quark free energy $F_Q(T, \mu_B)$. We compute the coefficients both for the expansion with $\mu_S = 0$, as well as along the strangeness neutral line $n_S = 0$. We demonstrate the convergence of the series by correctly predicting F_Q at imaginary μ_B in both cases. After discussing the renormalization of F_Q we will be in the position to calculate S_Q at finite density and determine its peak position as a function of μ_B.

A. Extrapolation of the static quark free energy

Since the renormalization of F_Q is additive and μ_B independent, the μ_B derivatives of F_Q do not require further treatment. We proceed to formulate a generic chain rule to calculate derivatives with respect to a quark chemical potential μ_j that corresponds to the up, down or strange quarks, with $j = u, d, s$, respectively. We will express the observables in temperature units. Thus, our actual expansion parameters are $\hat{\mu}_j = \mu_j/T$.

The chemical potential dependence is encoded in the quark determinants that appear in the staggered path integral

$$Z = \int \mathcal{D}U e^{-S_g(U)} \cdot \det M_u(U, m_l, \hat{\mu}_u)^{1/4} \cdot \det M_d(U, m_l, \hat{\mu}_d)^{1/4} \cdot \det M_s(U, m_s, \hat{\mu}_s)^{1/4} \quad (4)$$

where S_g is the gauge action, and $m_l = m_u = m_d$, m_s refer to the light and strange quark masses respectively. Up and down quarks are assumed to be degenerate. For a generic treatment we keep the chemical potentials for the two light quarks separate, in order to allow for nonzero isospin or electric charge chemical potential, though these are not considered in the present work.

It is useful to write each determinant's expansion as

$$\log\det M_j^{1/4}(U, m_j, \mu_j) = \log\det M_j^{1/4}(U, m_j, 0) + A_j\mu_j + \frac{1}{2!}B_j\mu_j^2 + \frac{1}{3!}C_j\mu_j^3 + \ldots \quad (5)$$

where there is no summation over the index j.

The chain rule that determines the extrapolation of an arbitrary variable X, following Ref. [43], reads

$$\partial_j\langle X\rangle = \langle XA_j\rangle - \langle X\rangle\langle A_j\rangle + \langle\partial_j X\rangle, \quad (6)$$

$$\partial_k\partial_j\langle X\rangle = \frac{1}{2}\langle XA_jA_k\rangle - \frac{1}{2}\langle X\rangle\langle A_jA_k\rangle - \langle XA_j\rangle\langle A_k\rangle + \langle X\rangle\langle A_k\rangle\langle A_j\rangle + \langle(\partial_k X)A_j\rangle - \langle\partial_k X\rangle\langle A_k\rangle + \frac{1}{2}\langle\partial_k\partial_j X\rangle - \frac{1}{2}\langle X\rangle\langle\partial_k A_j\rangle + (j \leftrightarrow k), \quad (7)$$

where ∂_j stands for $\partial/\partial\hat{\mu}_j$. Equation (5) implies that $\partial_k A_j = \delta_{jk}B_j$. The second equation is obtained through repeated application of the first one. This chain rule has already been the basis of numerous computations of various fluctuations of conserved charges in lattice QCD [43].

The application of this procedure to the Polyakov loop is straightforward, by applying Eq. (6) separately to its real and imaginary parts. This separation is useful when considering their different symmetry features. The odd terms $A, C, \ldots$, as well as $P_I = i\mathrm{Im}P$ are imaginary and odd under charge conjugation. On the other hand $B, D, \ldots$, as well as $P_R = \mathrm{Re}P$ are even and real. In C-symmetric simulations (with $\mu_B = 0$) where we calculate the Taylor coefficients, all odd expectation values vanish, e.g. $\langle A_j\rangle = 0$, $\langle A_jP_R\rangle = 0$, and $\langle B_jP_I\rangle = 0$. Being a purely gauge observable, the Polyakov loop on a given gauge configuration is independent of the chemical potentials. Hence $\partial_j P_R = \partial_j P_I \equiv 0$.

A straightforward application of these rules yields up to second order

$$\partial_j\langle P_R\rangle|_{\mu\equiv 0} = 0, \quad (8)$$

$$\partial_j\langle P_I\rangle|_{\mu\equiv 0} = \langle A_jP_I\rangle, \quad (9)$$

$$\partial_j\partial_k\langle P_R\rangle|_{\mu\equiv 0} = \delta_{jk}[\langle B_jP_R\rangle - \langle B_j\rangle\langle P_R\rangle] \times \langle A_jA_kP_R\rangle - \langle A_jA_k\rangle\langle P_R\rangle, \quad (10)$$

$$\partial_j\partial_k\langle P_I\rangle|_{\mu\equiv 0} = 0. \quad (11)$$

These can be combined into the following relation:

$$\frac{1}{2}\partial_j\partial_k|\langle P\rangle|^2 = +\delta_{jk}[\langle P_R\rangle\langle B_jP_R\rangle - \langle P_R\rangle^2\langle B_j\rangle] + \langle P_R\rangle\langle A_jA_kP_R\rangle - \langle A_jP_I\rangle\langle A_jP_I\rangle - \langle A_jA_k\rangle\langle P_R\rangle^2, \quad (12)$$

which, at the level of the static quark free energy, reads

$$\partial_j\partial_k F_Q = -\frac{T}{\langle P_R\rangle^2}\frac{1}{2}\partial_j\partial_k|\langle P\rangle|^2. \quad (13)$$

Equations (12) and (13) have been first formulated and used by the Pisa group in Ref. [38]. To our knowledge, higher order derivatives have never been addressed.

For the derivation of higher orders we have set up two independent automated procedures, so that they can be

cross-checked. In the first approach we have built a computer algebra program (in C language) that applies the chain rule and the symmetry rules. In the second setup a Python code has implemented combinatorial considerations short-cutting the tedious sequential derivatives. Both programs generated an identical computer code that was then used to calculate the numerical values of the coefficients. Examples of the formulas are given in Appendix B.

All combinations of quark chemical potentials have been computed. From these we constructed the generic derivatives (up to eighth order) in the μ_B-μ_S basis. Then, we could construct the expansion in μ_B both at $\mu_S = 0$, as well as on the strangeness neutral line. In the latter case, μ_S itself is subject to a Taylor expansion:

$$\hat{\mu}_S(\hat{\mu}_B) = s_1\hat{\mu}_B + s_3\hat{\mu}_B^3 + s_5\hat{\mu}_B^5 + s_7\hat{\mu}_B^7 + \ldots \quad (14)$$

We presented the continuum extrapolations for the first three coefficients in Ref. [40]. The formulas related to this expansion have been published by the HotQCD group [44].

The final expansion of F_Q is given in terms of the F_n coefficients defined as

$$F_Q(T,\mu_B) = -\frac{T}{2}\log|\langle P\rangle|^2 = F_Q(T,\mu_B=0) + T\sum_{n=2,4,\ldots}\frac{F_n}{n!}\left(\frac{\mu_B}{T}\right)^n. \quad (15)$$

We relate the expansion of $|P|^2$ to that of F_Q with the straightforward formulas (B1)–(B6) in Appendix B.

B. Expansion coefficients from the lattice

The sign problem appears in high order expansion coefficients in the form of large cancellations between competing terms. These lead to signal-to-noise ratios that are suppressed proportionally to the volume, by an additional factor for each subsequent order. This has forced us to reduce the volume to $16^3 \times 8$ for the scope of this study, and to work with extreme statistics of the order of $\mathcal{O}(10^6)$ configurations. The accumulated statistics and simulation parameters are listed in Appendix A. We use ensembles with 4HEX staggered fermions as in our recent work [40]. However, the statistics is increased by 1 order of magnitude. A further ingredient we employed to enhance the signal-to-noise ratio is the application of four HEX smearing steps to the Polyakov loop. This noise-reducing step is irrelevant in the continuum limit, and does not alter the sensitivity of the Polyakov loop to the breaking of the center symmetry. A similar strategy of using smeared Polyakov loops as noise reduction was used in Ref. [23].

In Refs. [40,45,46] we have already benefited from the reduced matrix formalism [47] to obtain the configuration-specific expansion coefficients $A_j, B_j, \ldots$ in Eq. (5) to arbitrary order. The chemical potentials are consistently defined to correspond to exactly conserved charges following the definition in Ref. [48].

Thus, our approach is unlike the standard strategy to calculate these coefficients in lattice QCD, which relies on Gaussian random vectors [43,49]. The reduced matrix formalism defines a large matrix of size $(6N_s^3)^2$ as means of a deterministic computation of the fermion determinant. In our case, it is a 24576×24576 matrix. The knowledge of all eigenvalues ξ_i allows the evaluation of the fermion determinant in a closed formula for any quark chemical potential μ

$$\frac{\det M(\mu,m,U)}{\det M(0,m,U)} = e^{-3N_s^3\mu/T}\prod_{i=1}^{6N_s^3}\frac{\xi_i[m,U] - e^{\mu/T}}{\xi_i[m,U]-1}. \quad (16)$$

At vanishing μ one can readily obtain the coefficients by following simple derivation rules. For low orders one obtains

$$A = \frac{i}{4}\mathrm{Im}\sum_i\frac{1}{1-\xi_i}, \quad (17)$$

$$B = \frac{1}{4}\mathrm{Re}\sum_i\frac{-\xi_i}{(1-\xi_i)^2}, \quad (18)$$

$$C = \frac{i}{4}\mathrm{Im}\sum_i\frac{\xi_i(1+\xi_i)}{(1-\xi_i)^3}, \quad (19)$$

$$D = \frac{1}{4}\mathrm{Re}\sum_i\frac{\xi_i(\xi_i^2+4\xi_i+1)}{(1-\xi_i)^4}. \quad (20)$$

We have one such matrix for each of the two masses for every configuration. That means 42 million separate diagonalizations for this paper altogether. We compute the eigenvalues using a dense linear algebra package, MAGMA [50–52], on the LUMI supercomputer in Finland.

We present the F_n coefficients computed on our $16^3 \times 8$ lattice in Fig. 2. The red symbols correspond to the expansion in μ_B with $\mu_S = 0$, the blue data refer to the strangeness neutral case ($n_S = 0$). The second order coefficient was previously calculated in a combination of imaginary μ_B and Taylor approach with $\mu_S = 0$ in Ref. [38] (using the opposite sign convention). The results are very similar, even though the volume and the action are different. The other seven coefficients are presented here for the first time.

C. Consistency with imaginary μ_B data

Before we move on to the applications we perform a cross-check of the coefficients by comparing them to imaginary μ_B data. We obtained the F_n coefficients entirely from $\mu_B = 0$ simulations.

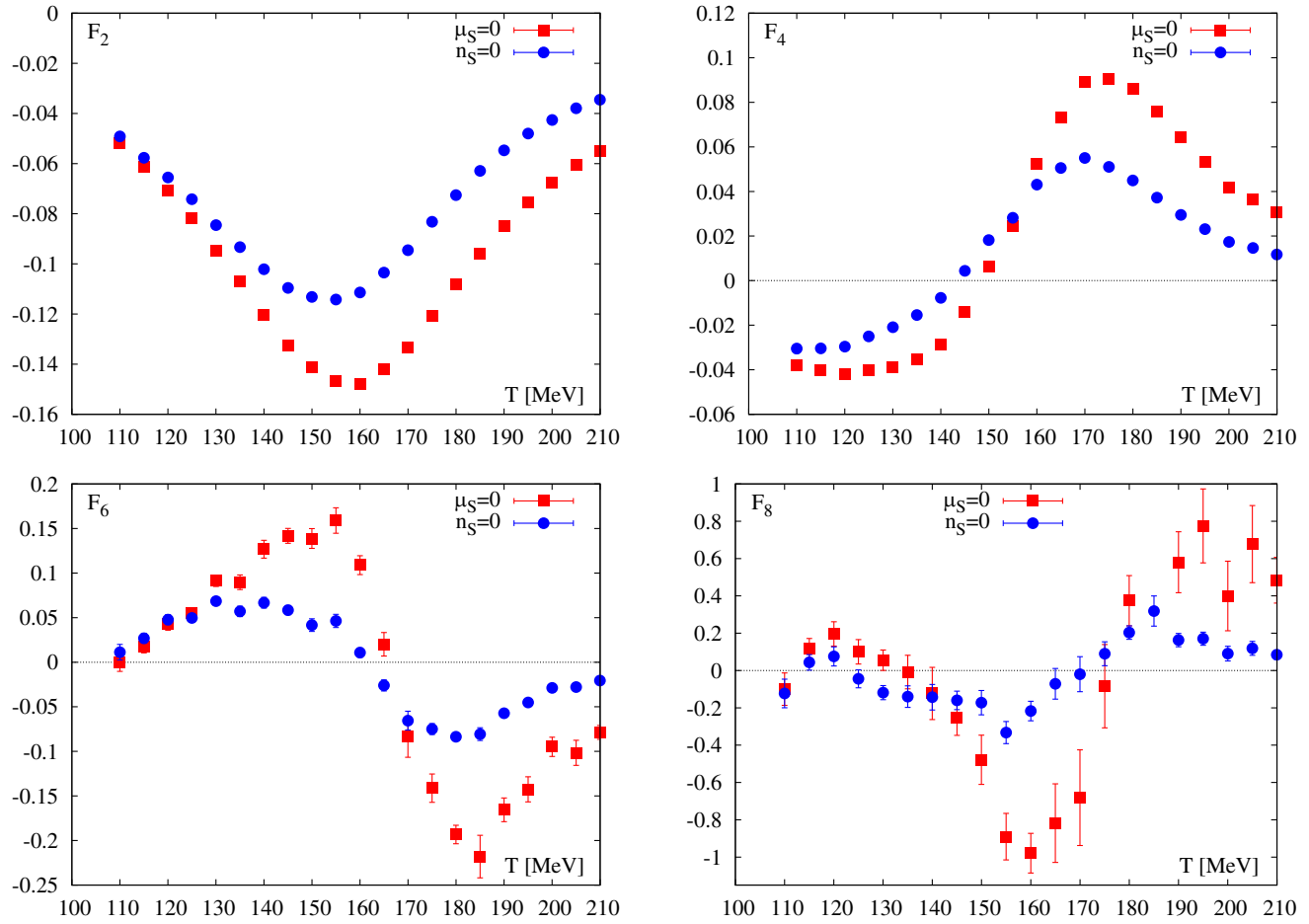

FIG. 2. Taylor coefficients of the static quark free energy in two setups: vanishing strangeness chemical potential in red, along strangeness neutral trajectories in blue.

For the sake of this cross-check we simulated at eight imaginary values of μ_B at $T = 140$ MeV, measuring the Polyakov loop in each run. By substituting imaginary values into our Taylor expansion we could make predictions on the imaginary μ_B runs' outcome.

In Fig. 3 we compare these predictions to the direct imaginary-μ_B simulations. The expansion produces reasonable predictions already at leading order as far as $\mu_B/T \sim i\pi/2$, and with higher orders it is compatible with the direct result up to $\mu_B/T \sim i\pi$. In that interval the eighth order gives only a small correction, thus demonstrating convergence.

As an additional check we compute the bare $F_Q(\mu_B)$ for imaginary chemical potentials. Since renormalization will only apply a constant shift to the entire plot, it plays no role for this comparison. In order to obtain direct data along the strangeness neutral line at imaginary μ_B, we reweighted each $\mathrm{Im}\mu_B > 0$ ensemble to the specific imaginary μ_S where $n_S = 0$. The target $\mu_S(\mu_B)$ was also computed using reweighting, with reweighting factors spread between 0.5 and 2. Even in the $n_S = 0$ scheme, our error bars are smaller than the symbol size. We stress that reweighting was only applied to the imaginary μ_B data and only for the sake of this crosscheck. We will refer to the resulting F_Q for both schemes as direct data, as opposed to the Taylor expansion, that is based on the $\mu_B = 0$ ensemble. We show the comparison in Fig. 4. For the phenomenologically more relevant strangeness neutral case ($n_S = 0$) we show four subsequent orders, while for the $\mu_S = 0$ expansion we plot the highest order only. Although the two expansion schemes clearly differ, each set of coefficients reproduce the respective direct dataset. Interestingly, the strangeness neutral extrapolation reaches a better agreement with direct data, and has smaller statistical noise. We observe a monotonic convergence for μ_B/T up to $i\pi$.

D. Renormalization at $\mu_B = 0$

The renormalization of the Polyakov loop, or that of F_Q, can be discussed independently of our extrapolation, and its details have already been worked out in the literature. The various methods can be classified into three approaches:

(i) The direct method exploits the fact that the difference of F_Q between two temperatures is finite,

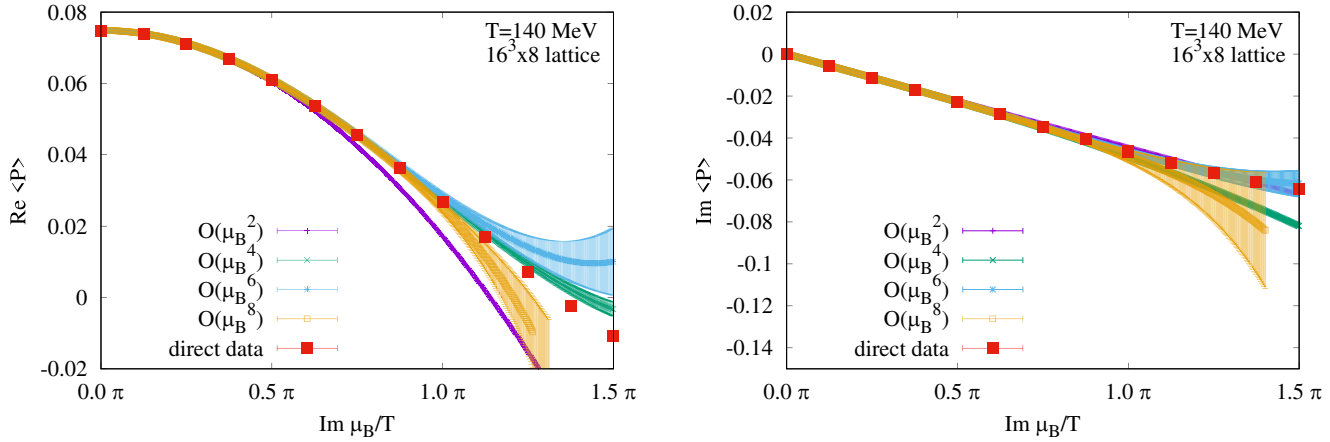

FIG. 3. The Taylor coefficients are used to extrapolate the bare Polyakov loop expectation value from $\mu_B = 0$ to imaginary values of the baryochemical potential. (Left: real part, right: imaginary part.) We demonstrate the convergence of the series at $T = 140$ MeV by comparing orders of the extrapolations (bands) to directly measured expectation values at $\mathrm{Im}\mu_B > 0$ from a separate set of simulations.

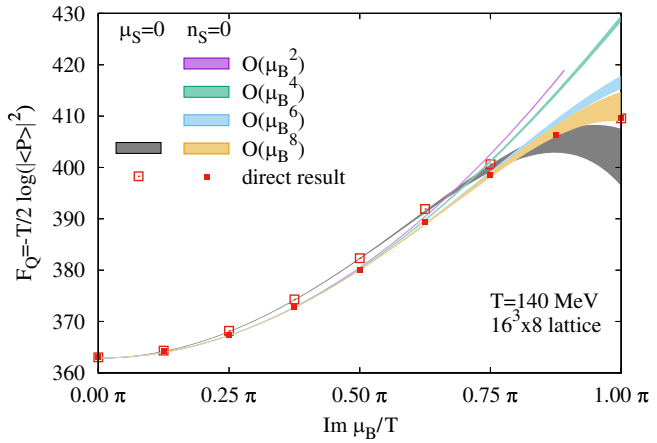

FIG. 4. The Taylor coefficients are used to extrapolate the bare static quark free energy (F_Q) from $\mu_B = 0$ to imaginary values of the baryochemical potential. We show the comparison both for the $\mu_S = 0$ as well as the $n_S = 0$ case. The respective expansion reproduces the direct data very well.

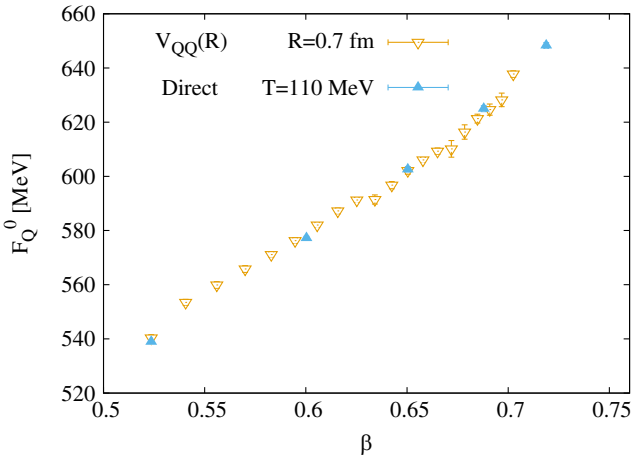

FIG. 5. We use two different approaches to the renormalization of the Polyakov loop. The full triangles correspond to the direct method (i), the open triangles are based on zero temperature simulations of Wilson loops (ii). The two datasets are shifted by a constant value so that their agreement is apparent.

if the two simulations used the same bare parameters [23,53].

(ii) The static quark potential ($V_{Q\bar{Q}}$) uses $T = 0$ simulations and relates the renormalization of $V_{Q\bar{Q}}$ to that of F_Q [53,54] or to the finite temperature heavy quark potential at small distances [55].

(iii) The Polyakov loop is finite at fixed finite gradient flow time [25,56,57].

In Fig. 5 we show the gauge coupling (β) dependence of the renormalization constant $F_Q^{(0)}(\beta)$ for schemes (i) and (ii). For option (iii) the flow time should be at a shorter length scale than other physical scales, yet it should also be above the scale of the lattice spacing. Given that the separation of these scales for $N_t = 8$ is not clear enough to endorse a suitable choice for flow time, we did not consider this approach.

For (i) we simulated a fixed temperature $T^* = 110$ MeV on a range of lattice resolutions $N_t = 8$, 10, 12, 14, and 16. The lattice spacing of the $N_t = 16$ ensemble at T^* corresponds to 220 MeV for $N_t = 8$. Thus, these five ensembles conveniently cover the entire range where renormalization is required. Then, $F_Q^0(\beta)$ is obtained as (an arbitrary constant plus) the measured bare F_Q from this setup. Other choices for T^* are possible, as the resulting renormalized F_Q would then differ by $\mathcal{O}(a^2)$ discretization errors only. However, larger values of T^* would force us to use $N_t = 6$ lattices that may have insufficient resolution. At smaller T^* the Polyakov loop is even smaller since then we are deep in the confined phase. It is a challenge then to keep the signal-to-noise ratio high enough, let alone that in that case an $N_t = 20$ ensemble would also be required to span the full β range.

For (ii) we simulated one $32^3 \times 64$ dedicated ensemble for each finite temperature run with a statistics of ≈1000 configurations in each. The 4HEX-smeared Wilson loops were calculated with additional spatial smearing (128 stout steps). We followed the standard procedure to extract and fit the effective mass from the time separation dependence of the Wilson loop and interpret these as $V_{Q\bar{Q}}(R)$, where R is the fixed spatial separation. Due to the 4HEX smearing the Cornell potential is distorted at small distance, so we fitted a generic rational function on $V_{Q\bar{Q}}(R)$ to interpolate at each gauge coupling to the same physical scale. Using a fixed $R = 0.7$ fm scale $V_{Q\bar{Q}}(R)/2$ gives the β-dependent renormalization factors. The factor $1/2$ comes from the forward and backward occurrence of the timelike line within the Wilson loop.

The $F_Q^0(\beta)$ counterterms slightly differ in the two methods. Their deviation is considered as one of the sources of systematic errors on $S_Q(T, \mu_B)$.

III. THE PHASE DIAGRAM

A. Deconfinement at finite μ_B

In the previous section we have worked out the expansion coefficients of the static quark free energy F_Q in μ_B/T and also computed it at zero chemical potential with two different renormalization methods. In short, we express $F_Q(T, \mu_B)$ as the difference of two terms

$$F_Q(T, \mu_B) = F_Q^{\text{bare}}(T, \mu_B) - F_Q^{\text{c.t.}}(T). \tag{21}$$

$$F_Q^{\text{bare}}(T, \mu_B) = F_Q^{\text{bare}}(T, 0) + T \sum_{n=2,4,\ldots} \frac{F_n}{n!} \left(\frac{\mu_B}{T}\right)^n. \tag{22}$$

Here the counterterm $F_Q^{\text{c.t.}}$ that was originally defined as a function of the gauge coupling (β) is rewritten as a function of temperature ($T = 1/(aN_t)$) using the $a(\beta)$ scale setting. The $a(\beta)$ function for this action was introduced in Ref. [40].

We start with the presentation of the renormalized Polyakov loop, since most readers are more familiar with this observable than F_Q or S_Q. Since we have already established F_Q at finite μ_B we define the renormalized Polyakov loop as $P^r = \exp\{-(F_Q - \Delta)/T\}$, where Δ sets the scheme. This means that for observables in this paper we always expand F_Q, not P_R or P_I. We choose Δ such that $P^r(T = 160\ \text{MeV}, \mu_B = 0) = 1$ as we did in Ref. [39]. The Polyakov loop curves are shown in Fig. 6. In the bottom panel of this figure, we also show the fourth, sixth and eighth order curves for $T = 130$ MeV. The expansion is under control below $\mu_B \approx 400$ MeV.

One could be tempted to define a proxy for the deconfinement transition via a constant value of P^r or F_Q. While one can construct such contours with little effort, their curvature will be less than that of the chiral transition

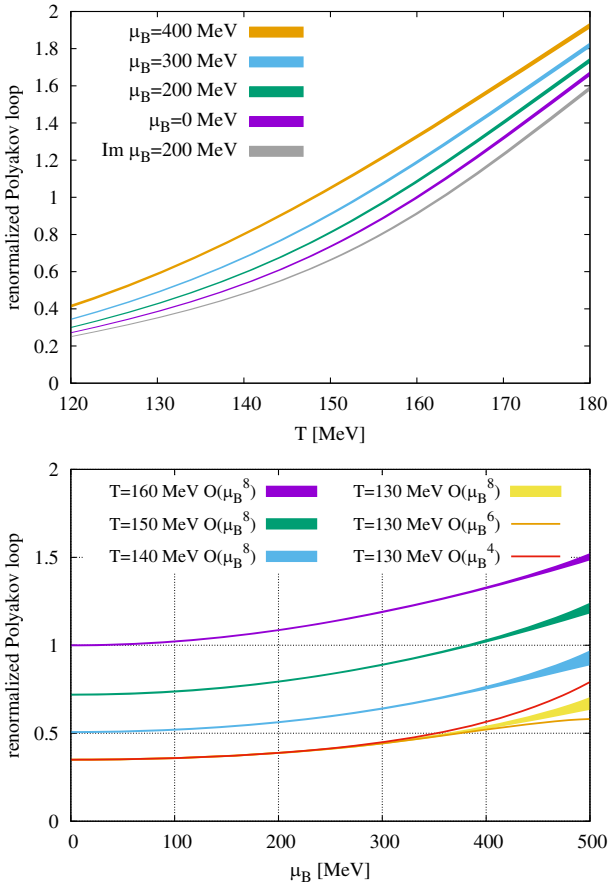

FIG. 6. Top: renormalized Polyakov loop (P^r) as a function of the temperature for various real chemical potentials, in the scheme defined by $P^r(T = 160\ \text{MeV}, \mu_B = 0) = 1$. The extrapolations are to eighth order in F_Q. We added the result with an imaginary chemical potential for comparison (gray line). Bottom: the same information, shown as a function of μ_B with fixed T. For one of the temperatures we show the fourth and sixth order results. The sixth order does not visibly differ from the full computation below $\mu_B = 350$ MeV.

line. We have shown this in Ref. [39], where F_Q and the chiral observables were compared at imaginary μ_B. Along the transition line $T_c(\mu_B)$, F_Q showed a statistically significant slope as a function of μ_B^2.

In this work, however, we focus on $S_Q(T, \mu_B)$. Its maximum corresponds to the inflection point of $F_Q(T)$. It is challenging to reach the precision needed to extract the second derivative with numerical differentiation. In Ref. [39] we have already accomplished this for several volumes and chemical potentials. We modelled the temperature dependence with a rational function, from which the inflection point was determined.

In Fig. 7 we show $S_Q(T)$ as defined in Eq. (3). The derivative was calculated by choosing a suitable interpolation of the two terms in Eq. (21), keeping μ_B fixed in MeV. We also show $S_Q(T)$ for one imaginary value of μ_B for comparison. The $S_Q(T)$ curves show two trends very

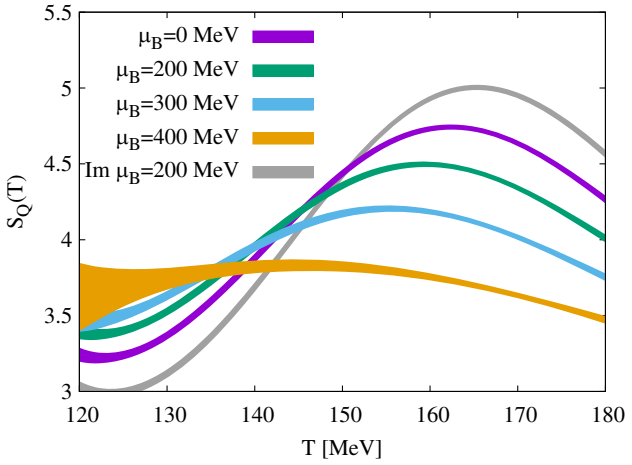

FIG. 7. The static quark entropy $[S_Q(T)]$ extrapolated to various chemical potentials. The errors in this plot are statistical only. We added one imaginary chemical potential (gray band) to better visualize the trend in μ_B.

clearly. First, the change in the peak position indicates the chemical potential dependence of the transition temperature. Second, the width of the peak increases as μ_B grows, indicating a weakening of the deconfinement transition. At the largest value of μ_B, the curve is the flattest. This feature contributes to the difficulty in determining the deconfinement temperature at large μ_B, in addition to the growing errors from the extrapolation. On the other hand, in the opposite (imaginary) direction, the peak is higher and narrower, eventually becoming singular in the Roberge-Weiss point [58].

B. Systematic analysis

In the following we describe the analysis procedure that allows us to draw the transition line in the phase diagram based on S_Q.

Renormalization introduces a lattice-spacing dependent shift of F_Q. This function is interpolated to the actual spacing that realizes a given temperature [$a = 1/(N_t T)$ with $N_t = 8$]. The interpolation of the same data to various temperature points introduces correlations between temperatures. To avoid this, we model the renormalization function $F_Q^{\text{c.t.}}(T)$ in Fig. 5 with a polynomial, independently from $F_Q^{\text{bare}}(T)$.

F_Q^{bare} is calculated at each value of μ_B (not μ_B/T) as a function of the temperature, by simply summing the Taylor series to eighth order [Eq. (22)]. This extrapolated data correspond to the would-be simulation result as if we simulated at finite μ_B. Each data point corresponds to a definite pair of T and μ_B. There is no statistical correlation between results at different temperatures, since each was obtained from a single $\mu_B = 0$ ensemble. We fit F_Q^{bare} with a rational function for every μ_B separately, in order to calculate its T derivative, namely $S_Q(T)$. In this work we used (3, 2), (i.e., cubic over quadratic) or (3, 3) (i.e., cubic over cubic) rational functions. The renormalized $S_Q(T)$ function is simply the difference of the temperature derivative of the rational function and that of $F_Q^{\text{c.t.}}(T)$. The maximum of $S_Q(T)$ for fixed μ_B is found without further modeling of the function.

The determination of the inflection point and the renormalization of F_Q are both procedures where ambiguous choices have to be made. We identified five such steps, and we use two alternative versions for each. Thus, there are a total of 32 $S_Q(T, \mu_B)$ curves for each μ_B value. In short, they include: (i) whether to apply a polynomial model for $F_Q^{\text{c.t.}}(\beta)$ or for $F_Q^{\text{c.t.}}(T)$ using the scale function $a(\beta)$ to convert between the two options, (ii) whether to fit these counterterm functions with third or fourth order polynomials, (iii) whether to use the zero or finite temperature data set to renormalize, (iv) two different ranges for the rational model of the bare F_Q, and finally (v) whether to use (3, 2) or (3, 3) rational approximations in T for $F_Q^{\text{bare}}(T, \mu_B)$. The systematic error is calculated with the histogram method of Ref. [59].

Once $S_Q(T, \mu_B)$ is known, its peak position gives the deconfinement crossover curve in the phase diagram. This is shown in the left panel of Fig. 1, with all of the systematic errors included. Furthermore, we can define the width of the transition as

$$\Delta T(\mu_B) = \sqrt{-S_Q(T,\mu_B) \Big/ \left.\frac{\partial^2 S_Q(T,\mu_B)}{\partial T^2}\right|_{T=T_c(\mu_B)}}. \tag{23}$$

In Ref. [34] an analogous definition was given for the full chiral susceptibility. While in Ref. [34] we constructed a proxy using the chiral condensate, here data quality allows us to directly compute the second derivative of S_Q at $T_c(\mu_B)$. For simplicity, we refitted the $S_Q(T, \mu_B)$ function at the peak of $S_Q(T)$ in two different ranges ($T_c \pm 10$ MeV and $T_c \pm 15$ MeV). With this sixth step the number of analyses totals 64. The resulting curve in the strangeness neutral case is shown in the right panel of Fig. 1. Already at $\mu_B = 0$, the width defined with S_Q is considerably larger than the chiral width. Furthermore, unlike the chiral width, which is approximately a constant at small chemical potentials, the deconfinement width gets larger with increasing μ_B, indicating a weakening crossover transition. One possible interpretation of this fact is that it is due to the increased distance from the Roberge-Weiss critical point [58]. A widening crossover implies that the existence of a critical point in this region is disfavored by the results of our analysis.

C. The role of strangeness neutrality

We finally discuss the impact of strangeness neutrality. In Fig. 8 we show the deconfinement transition line with the

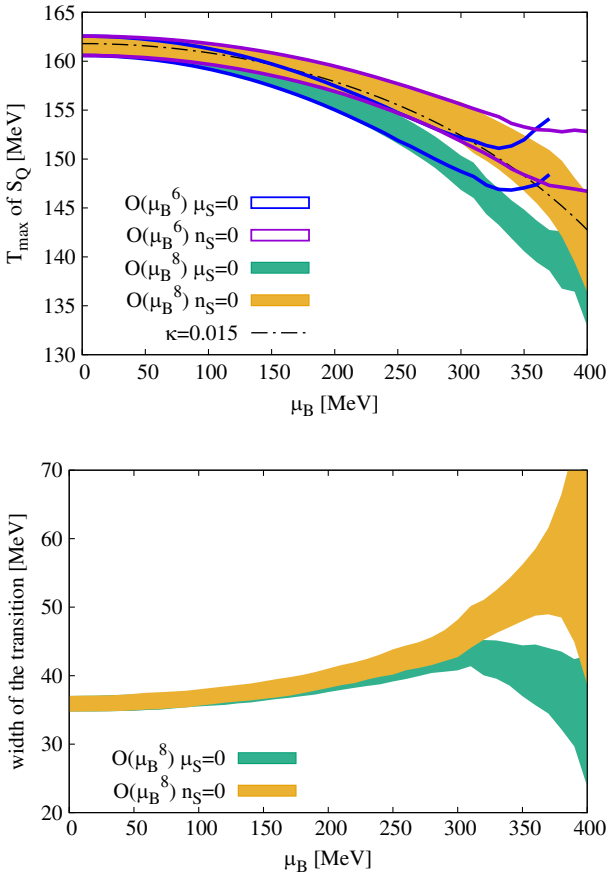

FIG. 8. Top: the maximum position of $S_Q(T)$ for fixed baryochemical potential (μ_B). We show both setups with ($n_S = 0$) and without ($\mu_S = 0$) strangeness neutrality. We quote a rounded value of the curvature of the chiral transition and show the corresponding transition line for further guidance. We also show the sixth order result on the phase diagram. The eighth order is clearly significant above 350 MeV. Bottom: the width of the transition defined as Eq. (23). While the width is similar for the strangeness neutral and in the $\mu_S = 0$ case we see a hint for a strengthening for $\mu_S = 0$ at the highest chemical potentials.

two standard choices: the simple extrapolation in μ_B keeping $\mu_S = 0$, and the strangeness neutral case $n_S = 0$. The latter was shown in our final result in Fig. 1. Since the simpler condition $\mu_S = 0$ is often used in lattice studies, we present a comparison here. (For recent estimates of the critical end point's possible location in the $\mu_S = 0$ scheme see Refs. [32,60,61]).

Similarly to the chiral transition line, the maximum of S_Q is also well approximated by the quadratic ansatz

$$T_c(\mu_B) = T_c(0)\left(1 - \kappa\frac{\mu_B^2}{T_c^2(\mu_B)}\right) \tag{24}$$

that we plot together with our lattice result to guide the eye. We used the rounded value of $\kappa = 0.015$. For specific extrapolation schemes, more precise values have been determined from lattice simulations [17,34,62–65]. The transition lines in Fig. 8 indicate a stronger curvature for the $\mu_S = 0$ case, as expected.

The second panel in Fig. 8 shows the differences in the width of the S_Q peak. While we see a steady increase in the width, i.e., a weakening of the deconfinement transition in the $n_S = 0$ case, the $\mu_S = 0$ shows a remarkable turn of this trend above 300 MeV. Given this behavior in Fig. 8 one can speculate if the width continues to drop, perhaps even down to zero. This would be consistent with the critical end point existent scenario. One could speculate that such reversal of the trend can also happen to the $n_S = 0$ width at a higher μ_B, but the error on our results at $\mu_B > 400$ MeV is too large to explore this possibility.

Note that this effect of the transition first weakening and then strengthening again is reminiscent of results from early work on the phase diagram on coarse staggered lattices [66–68].

Finally, we address the robustness of the present computation. We use the eighth order of the Taylor series, which may seem a very arbitrary decision. In fact, the order of the expansion was only limited by the statistics. In Fig. 8 we added the $\mathcal{O}(\mu_B^6)$ order version of our extrapolated transition lines, too. Up to 300 MeV the effect of the eighth order is invisible, and only gets statistically significant above $\mu_B \simeq 350$ MeV. For the $\mu_S = 0$ scheme the onset of the eighth order appears 50 MeV earlier. It is safe to claim that up to $\mu_B \leq 300$ MeV the systematic errors from the truncated extrapolation can be completely neglected, and we give a fair description of finite volume QCD at finite μ_B. At the same time, the eighth order is the lowest possible truncation in the range 300–400 MeV. Lower orders cannot give reliable results. The difference in the width between the $n_S = 0$ and $\mu_S = 0$ schemes is an effect that is visible only if the eighth order is included.

IV. CONCLUSIONS

We studied the crossover line on the QCD phase diagram in an unprecedented range of chemical potentials. We complemented previous lattice results on the chiral aspects of the QCD transition by focusing on observables that are associated with deconfinement.

We calculated the Polyakov loop and the static quark free energy in hot and dense QCD as functions of T and μ_B. Direct simulations at finite μ_B are hindered by the sign problem, but various expansion techniques exist to extrapolate the results to finite density. Here we employed the Taylor method using an eighth order expansion in the baryochemical potential-to-temperature ratio μ_B/T.

The Taylor method, which is often used to extrapolate the QCD pressure, is known to suffer from a remnant sign problem: the positive and negative terms (e.g. those we list in Appendix B) exhibit a cancellation. This sign problem worsens with each subsequent order of the expansion with a volume dependent factor. Although the sixth and eighth

order coefficients of the pressure are often studied in the literature, the errors are large.

The novelty in this work is the extension of the Taylor scheme to the Polyakov loop and related observables. While this step posed no conceptual challenge, the derivation and implementation of the high order coefficients would have been a formidable task without the use of a computer algebra system that we developed for the purpose. We note that no new lattice measurements had to be implemented in the simulation code other than the Polyakov loop itself and the standard routines that are required for the expansion of the pressure.

Yet, the most important ingredient that has allowed us to reach 400 MeV in the baryochemical potential was the selection of a simulation volume that keeps the sign problem under control. Indeed, the errors on the expansion coefficients in this work are a fraction of those that are often used in large volume simulations (e.g. for the pressure). Finite volume effects are not negligible, but were quantified in a previous work, and found to be small. While chiral observables suffer from large finite volume corrections, the Polyakov loop is much less sensitive. The aspect ratio of $N_x/N_t = L \cdot T = 2$ is a choice that allows a wider opening of our window in the QCD phase diagram.

Simulating with extreme statistics (>1 million configurations) at each temperature in a finite volume we calculated the bare Polyakov loop in the entire range covered by the Beam Energy Scan program in collider mode. This bare Polyakov loop would have been the direct result if simulations at finite μ_B were possible.

We defined the transition line as the peak of the static quark entropy. For this we used a renormalization procedure that has already been extensively discussed in the literature.

The transition line in this work could be extended up to 400 MeV in the baryochemical potential. It closely follows the chiral crossover line, though the latter is known with larger errors and in a smaller range.

With this result the phenomenological freeze-out line can be compared to the deconfinement line in a longer range than before. In particular, we cover the full range of the STAR freeze-out determination of Ref. [41].

The curvature of the static quark entropy at its peak can be used to define a width parameter for the deconfinement crossover. We showed that up to $\mu_B \approx 400$ MeV, the width parameter is getting larger at larger μ_B. This disfavors the existence of a deconfinement critical endpoint in this regime.

Finally, we compared the phenomenologically more relevant case of strangeness neutral matter with the theoretically more easily tractable case of zero strangeness chemical potential. While the curvature of the $T_c(\mu_B)$ curve is slightly smaller for the strangeness neutral case, the width parameters are consistent (within error) up to $\mu_B \approx 300$ MeV. In the range 300 MeV $< \mu_B <$ 400 MeV, there is a difference in the width parameters, with the $\mu_S = 0$ curve apparently turning around and showing a narrowing of the transition (at least to this order in the Taylor expansion). This behavior might be caused by a critical end point beyond $\mu_B = 400$ MeV. One might speculate that such a narrowing can also happen to the $n_S = 0$ transition, but at higher values of μ_B. Unambiguously deciding whether this is the case calls for further investigations.

ACKNOWLEDGMENTS

The project was supported by the BMBF Grant No. 05P21PXFCA. This work is also supported by the MKW NRW under the funding code NW21-024-A. Further funding was received from the DFG under the Project No. 496127839. This work was also supported by the Hungarian National Research, Development and Innovation Office, NKFIH Grant No. KKP126769. This work was also supported by the NKFIH excellence grant TKP2021_NKTA_64. This work is also supported by the Hungarian National Research, Development and Innovation Office under Project No. FK 147164. The authors gratefully acknowledge the Gauss Centre for Supercomputing e.V. [69] for funding this project by providing computing time on the GCS Supercomputer Juwels-Booster at Juelich Supercomputer Centre and on Hawk, at HLRS Stuttgart. We acknowledge the EuroHPC Joint Undertaking for awarding this project access to the EuroHPC supercomputer LUMI, hosted by CSC (Finland) and the LUMI consortium through a EuroHPC Extreme Access call.

DATA AVAILABILITY

No data were created or analyzed in this study.

APPENDIX A: STATISTICS AND PARAMETERS

In this work we use 21 finite temperature ensembles to calculate the F_Q coefficients, as listed in Table I. For each configuration we computed all eigenvalues of the reduced matrix for both the light and the strange quark masses. The first and the last temperatures were actually excluded from the analysis.

In addition, four more ensembles were generated on the same line of constant physics using $20^3 \times 10$, $24^3 \times 12$, $28^3 \times 28$ and $32^3 \times 16$ for the direct renormalization of the Polyakov loop. For the $V_{Q\bar{Q}}$-based renormalization zero temperature ensembles ($32^3 \times 64$ lattice) were generated for the entire list with 1000 configurations in each.

TABLE I. Simulation parameters on the $16^3 \times 8$ lattice and the number of configurations where the static quark potential's μ derivatives have been computed. The parameters are unchanged since Ref. [40]. The statistics have been increased by one order of magnitude.

T [MeV]	β	m_l	m_s	No. of configurations
110	0.5236	0.00432111	0.1193920	410816
115	0.5406	0.00409845	0.1132400	1036373
120	0.5560	0.00390982	0.1080280	1080141
125	0.5700	0.00374705	0.1035310	1500967
130	0.5829	0.00360381	0.0995733	1887321
135	0.5947	0.00347548	0.0960274	1216195
140	0.6056	0.00335869	0.0928007	1912628
145	0.6158	0.00325107	0.0898270	1383987
150	0.6252	0.00315088	0.0870590	1338744
155	0.6341	0.00305689	0.0844619	1005178
160	0.6425	0.00296817	0.0820105	2215412
165	0.6504	0.00288403	0.0796857	1596043
170	0.6579	0.00280394	0.0774727	595253
175	0.6651	0.00272748	0.0753604	1131649
180	0.6719	0.00265434	0.0733394	1240884
185	0.6785	0.00258424	0.0714026	436002
190	0.6848	0.00251696	0.0695436	317895
195	0.6909	0.00245231	0.0677573	361870
200	0.6968	0.00239013	0.0660393	323968
205	0.7025	0.00233028	0.0643856	158703
210	0.7080	0.00227263	0.0627928	260064

APPENDIX B: EXPANSION FORMULAS FOR THE POLYAKOV LOOP

With the notations $Q = |\langle P\rangle|^2$ and $Q^{(n)} = d^n Q/d\hat{\mu}^n$ we can convert the expansion of the norm of the Polyakov loop into the static quark free energy:

$$F = -\frac{T}{2}\log|\langle P\rangle|^2 = T\sum_{n=0,2,\ldots}\frac{F_n}{n!}\left(\frac{\mu}{T}\right)^n \tag{B1}$$

$$F_0 = -\frac{1}{2}\log(Q) \tag{B2}$$

$$F_2 = -\frac{1}{2}\left[+\frac{Q^{(2)}}{Q}\right] \tag{B3}$$

$$F_4 = -\frac{1}{2}\left[+\frac{Q^{(4)}}{Q} - 3\frac{(Q^{(2)})^2}{Q^2}\right] \tag{B4}$$

$$F_6 = -\frac{1}{2}\left[+\frac{Q^{(6)}}{Q} - 15\frac{Q^{(2)}Q^{(4)}}{Q^2} + 30\frac{(Q^{(2)})^3}{Q^3}\right] \tag{B5}$$

$$F_8 = -\frac{1}{2}\left[+\frac{Q^{(8)}}{Q} - 35\frac{(Q^{(4)})^2}{Q^2} - 28\frac{Q^{(2)}Q^{(6)}}{Q^2} + 420\frac{(Q^{(2)})^2Q^{(4)}}{Q^3} - 630\frac{(Q^{(2)})^4}{Q^4}\right] \tag{B6}$$

In the following set of formulas we give the μ_u derivatives of the norm (Q) of the Polyakov loop. These can be easily converted into μ_B derivatives, if needed. For the full expansion all combinations of μ_u, μ_d and μ_s are needed, but we do not list them here. These few, however, should make cross-checks of future implementations possible. We remind the reader that the odd coefficients $A, C, \ldots$ are imaginary. Note that P_I is not the imaginary part, but i times the imaginary part of the Polyakov loop.

$$\begin{aligned}
\partial_u^2 Q = {} & +2\langle P_R\rangle\langle B_u P_R\rangle + 2\langle P_R\rangle\langle A_u A_u P_R\rangle - 2\langle A_u P_I\rangle\langle A_u P_I\rangle - 2\langle B_u\rangle\langle P_R\rangle\langle P_R\rangle - 2\langle A_u A_u\rangle\langle P_R\rangle\langle P_R\rangle \\
\partial_u^4 Q = {} & +2\langle P_R\rangle\langle D_u P_R\rangle + 6\langle P_R\rangle\langle B_u B_u P_R\rangle + 8\langle P_R\rangle\langle A_u C_u P_R\rangle + 12\langle P_R\rangle\langle A_u A_u B_u P_R\rangle + 2\langle P_R\rangle\langle A_u A_u A_u A_u P_R\rangle \\
& + 6\langle B_u P_R\rangle\langle B_u P_R\rangle - 8\langle A_u P_I\rangle\langle C_u P_I\rangle - 24\langle A_u P_I\rangle\langle A_u B_u P_I\rangle - 8\langle A_u P_I\rangle\langle A_u A_u A_u P_I\rangle + 12\langle A_u A_u P_R\rangle\langle B_u P_R\rangle \\
& + 6\langle A_u A_u P_R\rangle\langle A_u A_u P_R\rangle - 2\langle D_u\rangle\langle P_R\rangle\langle P_R\rangle - 24\langle B_u\rangle\langle P_R\rangle\langle B_u P_R\rangle - 24\langle B_u\rangle\langle P_R\rangle\langle A_u A_u P_R\rangle \\
& + 24\langle B_u\rangle\langle A_u P_I\rangle\langle A_u P_I\rangle - 6\langle B_u B_u\rangle\langle P_R\rangle\langle P_R\rangle - 8\langle A_u C_u\rangle\langle P_R\rangle\langle P_R\rangle - 24\langle A_u A_u\rangle\langle P_R\rangle\langle B_u P_R\rangle \\
& - 24\langle A_u A_u\rangle\langle P_R\rangle\langle A_u A_u P_R\rangle + 24\langle A_u A_u\rangle\langle A_u P_I\rangle\langle A_u P_I\rangle - 12\langle A_u A_u B_u\rangle\langle P_R\rangle\langle P_R\rangle - 2\langle A_u A_u A_u A_u\rangle\langle P_R\rangle\langle P_R\rangle \\
& + 18\langle B_u\rangle\langle B_u\rangle\langle P_R\rangle\langle P_R\rangle + 36\langle A_u A_u\rangle\langle B_u\rangle\langle P_R\rangle\langle P_R\rangle + 18\langle A_u A_u\rangle\langle A_u A_u\rangle\langle P_R\rangle\langle P_R\rangle
\end{aligned}$$

$$\begin{aligned}
\partial_u^6 Q = {} & +2\langle P_R\rangle\langle F_u P_R\rangle + 20\langle P_R\rangle\langle C_u C_u P_R\rangle + 30\langle P_R\rangle\langle B_u D_u P_R\rangle + 30\langle P_R\rangle\langle B_u B_u B_u P_R\rangle + 12\langle P_R\rangle\langle A_u E_u P_R\rangle \\
& + 120\langle P_R\rangle\langle A_u B_u C_u P_R\rangle + 30\langle P_R\rangle\langle A_u A_u D_u P_R\rangle + 90\langle P_R\rangle\langle A_u A_u B_u B_u P_R\rangle + 40\langle P_R\rangle\langle A_u A_u A_u C_u P_R\rangle \\
& + 30\langle P_R\rangle\langle A_u A_u A_u A_u B_u P_R\rangle + 2\langle P_R\rangle\langle A_u A_u A_u A_u A_u A_u P_R\rangle - 20\langle C_u P_I\rangle\langle C_u P_I\rangle + 30\langle B_u P_R\rangle\langle D_u P_R\rangle \\
& + 90\langle B_u P_R\rangle\langle B_u B_u P_R\rangle + 120\langle B_u P_R\rangle\langle A_u C_u P_R\rangle + 180\langle B_u P_R\rangle\langle A_u A_u B_u P_R\rangle - 12\langle A_u P_I\rangle\langle E_u P_I\rangle \\
& - 120\langle A_u P_I\rangle\langle B_u C_u P_I\rangle - 60\langle A_u P_I\rangle\langle A_u D_u P_I\rangle - 180\langle A_u P_I\rangle\langle A_u B_u B_u P_I\rangle - 120\langle A_u P_I\rangle\langle A_u A_u C_u P_I\rangle
\end{aligned}$$

$$
\begin{aligned}
&- 120\langle A_u P_I\rangle\langle A_u A_u A_u B_u P_I\rangle - 12\langle A_u P_I\rangle\langle A_u A_u A_u A_u A_u P_I\rangle - 120\langle A_u B_u P_I\rangle\langle C_u P_I\rangle - 180\langle A_u B_u P_I\rangle\langle A_u B_u P_I\rangle \\
&+ 30\langle A_u A_u P_R\rangle\langle D_u P_R\rangle + 90\langle A_u A_u P_R\rangle\langle B_u B_u P_R\rangle + 120\langle A_u A_u P_R\rangle\langle A_u C_u P_R\rangle + 180\langle A_u A_u P_R\rangle\langle A_u A_u B_u P_R\rangle \\
&+ 30\langle A_u A_u P_R\rangle\langle A_u A_u A_u A_u P_R\rangle - 40\langle A_u A_u A_u P_I\rangle\langle C_u P_I\rangle - 120\langle A_u A_u A_u P_I\rangle\langle A_u B_u P_I\rangle - 20\langle A_u A_u A_u P_I\rangle\langle A_u A_u A_u P_I\rangle \\
&+ 30\langle A_u A_u A_u A_u P_R\rangle\langle B_u P_R\rangle - 2\langle F_u\rangle\langle P_R\rangle\langle P_R\rangle - 60\langle D_u\rangle\langle P_R\rangle\langle B_u P_R\rangle - 60\langle D_u\rangle\langle P_R\rangle\langle A_u A_u P_R\rangle \\
&+ 60\langle D_u\rangle\langle A_u P_I\rangle\langle A_u P_I\rangle - 20\langle C_u C_u\rangle\langle P_R\rangle\langle P_R\rangle - 60\langle B_u\rangle\langle P_R\rangle\langle D_u P_R\rangle - 180\langle B_u\rangle\langle P_R\rangle\langle B_u B_u P_R\rangle \\
&- 240\langle B_u\rangle\langle P_R\rangle\langle A_u C_u P_R\rangle - 360\langle B_u\rangle\langle P_R\rangle\langle A_u A_u B_u P_R\rangle - 60\langle B_u\rangle\langle P_R\rangle\langle A_u A_u A_u A_u P_R\rangle - 180\langle B_u\rangle\langle B_u P_R\rangle\langle B_u P_R\rangle \\
&+ 240\langle B_u\rangle\langle A_u P_I\rangle\langle C_u P_I\rangle + 720\langle B_u\rangle\langle A_u P_I\rangle\langle A_u B_u P_I\rangle + 240\langle B_u\rangle\langle A_u P_I\rangle\langle A_u A_u A_u P_I\rangle - 360\langle B_u\rangle\langle A_u A_u P_R\rangle\langle B_u P_R\rangle \\
&- 180\langle B_u\rangle\langle A_u A_u P_R\rangle\langle A_u A_u P_R\rangle - 30\langle B_u D_u\rangle\langle P_R\rangle\langle P_R\rangle - 180\langle B_u B_u\rangle\langle P_R\rangle\langle B_u P_R\rangle - 180\langle B_u B_u\rangle\langle P_R\rangle\langle A_u A_u P_R\rangle \\
&+ 180\langle B_u B_u\rangle\langle A_u P_I\rangle\langle A_u P_I\rangle - 30\langle B_u B_u B_u\rangle\langle P_R\rangle\langle P_R\rangle - 12\langle A_u E_u\rangle\langle P_R\rangle\langle P_R\rangle - 240\langle A_u C_u\rangle\langle P_R\rangle\langle B_u P_R\rangle \\
&- 240\langle A_u C_u\rangle\langle P_R\rangle\langle A_u A_u P_R\rangle + 240\langle A_u C_u\rangle\langle A_u P_I\rangle\langle A_u P_I\rangle - 120\langle A_u B_u C_u\rangle\langle P_R\rangle\langle P_R\rangle - 60\langle A_u A_u\rangle\langle P_R\rangle\langle D_u P_R\rangle \\
&- 180\langle A_u A_u\rangle\langle P_R\rangle\langle B_u B_u P_R\rangle - 240\langle A_u A_u\rangle\langle P_R\rangle\langle A_u C_u P_R\rangle - 360\langle A_u A_u\rangle\langle P_R\rangle\langle A_u A_u B_u P_R\rangle \\
&- 60\langle A_u A_u\rangle\langle P_R\rangle\langle A_u A_u A_u A_u P_R\rangle - 180\langle A_u A_u\rangle\langle B_u P_R\rangle\langle B_u P_R\rangle + 240\langle A_u A_u\rangle\langle A_u P_I\rangle\langle C_u P_I\rangle \\
&+ 720\langle A_u A_u\rangle\langle A_u P_I\rangle\langle A_u B_u P_I\rangle + 240\langle A_u A_u\rangle\langle A_u P_I\rangle\langle A_u A_u A_u P_I\rangle - 360\langle A_u A_u\rangle\langle A_u A_u P_R\rangle\langle B_u P_R\rangle \\
&- 180\langle A_u A_u\rangle\langle A_u A_u P_R\rangle\langle A_u A_u P_R\rangle - 30\langle A_u A_u D_u\rangle\langle P_R\rangle\langle P_R\rangle - 360\langle A_u A_u B_u\rangle\langle P_R\rangle\langle B_u P_R\rangle \\
&- 360\langle A_u A_u B_u\rangle\langle P_R\rangle\langle A_u A_u P_R\rangle + 360\langle A_u A_u B_u\rangle\langle A_u P_I\rangle\langle A_u P_I\rangle - 90\langle A_u A_u B_u B_u\rangle\langle P_R\rangle\langle P_R\rangle \\
&- 40\langle A_u A_u A_u C_u\rangle\langle P_R\rangle\langle P_R\rangle - 60\langle A_u A_u A_u A_u\rangle\langle P_R\rangle\langle B_u P_R\rangle - 60\langle A_u A_u A_u A_u\rangle\langle P_R\rangle\langle A_u A_u P_R\rangle \\
&+ 60\langle A_u A_u A_u A_u\rangle\langle A_u P_I\rangle\langle A_u P_I\rangle - 30\langle A_u A_u A_u A_u B_u\rangle\langle P_R\rangle\langle P_R\rangle - 2\langle A_u A_u A_u A_u A_u A_u\rangle\langle P_R\rangle\langle P_R\rangle \\
&+ 90\langle B_u\rangle\langle D_u\rangle\langle P_R\rangle\langle P_R\rangle + 540\langle B_u\rangle\langle B_u\rangle\langle P_R\rangle\langle B_u P_R\rangle + 540\langle B_u\rangle\langle B_u\rangle\langle P_R\rangle\langle A_u A_u P_R\rangle \\
&- 540\langle B_u\rangle\langle B_u\rangle\langle A_u P_I\rangle\langle A_u P_I\rangle + 270\langle B_u\rangle\langle B_u B_u\rangle\langle P_R\rangle\langle P_R\rangle + 360\langle B_u\rangle\langle A_u C_u\rangle\langle P_R\rangle\langle P_R\rangle \\
&+ 540\langle B_u\rangle\langle A_u A_u B_u\rangle\langle P_R\rangle\langle P_R\rangle + 90\langle A_u A_u\rangle\langle D_u\rangle\langle P_R\rangle\langle P_R\rangle + 1080\langle A_u A_u\rangle\langle B_u\rangle\langle P_R\rangle\langle B_u P_R\rangle \\
&+ 1080\langle A_u A_u\rangle\langle B_u\rangle\langle P_R\rangle\langle A_u A_u P_R\rangle - 1080\langle A_u A_u\rangle\langle B_u\rangle\langle A_u P_I\rangle\langle A_u P_I\rangle + 270\langle A_u A_u\rangle\langle B_u B_u\rangle\langle P_R\rangle\langle P_R\rangle \\
&+ 360\langle A_u A_u\rangle\langle A_u C_u\rangle\langle P_R\rangle\langle P_R\rangle + 540\langle A_u A_u\rangle\langle A_u A_u\rangle\langle P_R\rangle\langle B_u P_R\rangle + 540\langle A_u A_u\rangle\langle A_u A_u\rangle\langle P_R\rangle\langle A_u A_u P_R\rangle \\
&- 540\langle A_u A_u\rangle\langle A_u A_u\rangle\langle A_u P_I\rangle\langle A_u P_I\rangle + 540\langle A_u A_u\rangle\langle A_u A_u B_u\rangle\langle P_R\rangle\langle P_R\rangle + 90\langle A_u A_u\rangle\langle A_u A_u A_u A_u\rangle\langle P_R\rangle\langle P_R\rangle \\
&+ 90\langle A_u A_u A_u A_u\rangle\langle B_u\rangle\langle P_R\rangle\langle P_R\rangle - 360\langle B_u\rangle\langle B_u\rangle\langle B_u\rangle\langle P_R\rangle\langle P_R\rangle - 1080\langle A_u A_u\rangle\langle B_u\rangle\langle B_u\rangle\langle P_R\rangle\langle P_R\rangle \\
&- 1080\langle A_u A_u\rangle\langle A_u A_u\rangle\langle B_u\rangle\langle P_R\rangle\langle P_R\rangle - 360\langle A_u A_u\rangle\langle A_u A_u\rangle\langle A_u A_u\rangle\langle P_R\rangle\langle P_R\rangle
\end{aligned}
$$

$\partial_u^8 Q =$ has 405 terms.

[1] Y. Aoki, G. Endrodi, Z. Fodor, S. Katz, and K. Szabo, Nature (London) **443**, 675 (2006).
[2] S. Borsanyi, Z. Fodor, C. Hoelbling, S. D. Katz, S. Krieg, C. Ratti, and K. K. Szabó, J. High Energy Phys. 09 (2010) 073.
[3] H. T. Ding *et al.* (HotQCD Collaboration), Phys. Rev. Lett. **123**, 062002 (2019).
[4] A. Bazavov, T. Bhattacharya, M. Cheng, C. DeTar, H. Ding *et al.*, Phys. Rev. D **85**, 054503 (2012).
[5] A. Y. Kotov, M. P. Lombardo, and A. Trunin, Phys. Lett. B **823**, 136749 (2021).
[6] F. Cuteri, O. Philipsen, and A. Sciarra, J. High Energy Phys. 11 (2021) 141.
[7] S. Pratt, E. Sangaline, P. Sorensen, and H. Wang, Phys. Rev. Lett. **114**, 202301 (2015).
[8] L.-G. Pang, K. Zhou, N. Su, H. Petersen, H. Stöcker, and X.-N. Wang, Nat. Commun. **9**, 210 (2018).
[9] M. Abdallah *et al.* (STAR Collaboration), Phys. Rev. Lett. **127**, 262301 (2021).
[10] R. D. Pisarski and F. Wilczek, Phys. Rev. D **29**, 338 (1984).
[11] A. Pelissetto and E. Vicari, Phys. Rev. D **88**, 105018 (2013).
[12] G. Fejos and T. Hatsuda, Phys. Rev. D **110**, 016021 (2024).
[13] Y. Aoki, Z. Fodor, S. Katz, and K. Szabo, Phys. Lett. B **643**, 46 (2006).

[14] Y. Aoki, S. Borsanyi, S. Durr, Z. Fodor, S. D. Katz, S. Krieg, and K. Szabo, J. High Energy Phys. 06 (2009) 088.
[15] S. Ejiri, F. Karsch, E. Laermann, C. Miao, S. Mukherjee *et al.*, Phys. Rev. D **80**, 094505 (2009).
[16] H. T. Ding *et al.*, Phys. Rev. Lett. **123**, 062002 (2019).
[17] H. T. Ding, O. Kaczmarek, F. Karsch, P. Petreczky, M. Sarkar, C. Schmidt, and S. Sharma, Phys. Rev. D **109**, 114516 (2024).
[18] S. Borsanyi, R. Kara, Z. Fodor, D. A. Godzieba, P. Parotto, and D. Sexty, Phys. Rev. D **105**, 074513 (2022).
[19] L. D. McLerran and B. Svetitsky, Phys. Rev. D **24**, 450 (1981).
[20] F. Cuteri, O. Philipsen, A. Schön, and A. Sciarra, Phys. Rev. D **103**, 014513 (2021).
[21] A. Bazavov, T. Bhattacharya, M. Cheng, N. Christ, C. DeTar *et al.*, Phys. Rev. D **80**, 014504 (2009).
[22] A. Bazavov and P. Petreczky, Phys. Rev. D **87**, 094505 (2013).
[23] S. Borsányi, Z. Fodor, S. D. Katz, A. Pásztor, K. K. Szabó, and C. Török, J. High Energy Phys. 04 (2015) 138.
[24] D. A. Clarke, O. Kaczmarek, F. Karsch, A. Lahiri, and M. Sarkar, Phys. Rev. D **103**, L011501 (2021).
[25] A. Bazavov, N. Brambilla, H. T. Ding, P. Petreczky, H. P. Schadler, A. Vairo, and J. H. Weber, Phys. Rev. D **93**, 114502 (2016).
[26] P. J. Gunkel and C. S. Fischer, Phys. Rev. D **104**, 054022 (2021).
[27] P. Kovács, Z. Szép, and G. Wolf, Phys. Rev. D **93**, 114014 (2016).
[28] F. Gao and J. M. Pawlowski, Phys. Rev. D **102**, 034027 (2020).
[29] W.-j. Fu, X. Luo, J. M. Pawlowski, F. Rennecke, R. Wen, and S. Yin, Phys. Rev. D **104**, 094047 (2021).
[30] P. Isserstedt, M. Buballa, C. S. Fischer, and P. J. Gunkel, Phys. Rev. D **100**, 074011 (2019).
[31] R. Critelli, J. Noronha, J. Noronha-Hostler, I. Portillo, C. Ratti, and R. Rougemont, Phys. Rev. D **96**, 096026 (2017).
[32] M. Hippert, J. Grefa, T. A. Manning, J. Noronha, J. Noronha-Hostler, I. Portillo Vazquez, C. Ratti, R. Rougemont, and M. Trujillo, Phys. Rev. D **110**, 094006 (2024).
[33] J. Adam *et al.* (STAR Collaboration), Phys. Rev. Lett. **126**, 092301 (2021).
[34] S. Borsanyi, Z. Fodor, J. N. Guenther, R. Kara, S. D. Katz, P. Parotto, A. Pasztor, C. Ratti, and K. K. Szabo, Phys. Rev. Lett. **125**, 052001 (2020).
[35] C. Bonati, M. D'Elia, F. Negro, F. Sanfilippo, and K. Zambello, Phys. Rev. D **98**, 054510 (2018).
[36] A. Bazavov *et al.* (HotQCD Collaboration), Phys. Lett. B **795**, 15 (2019).
[37] A. Pásztor, Z. Szép, and G. Markó, Phys. Rev. D **103**, 034511 (2021).
[38] M. D'Elia, F. Negro, A. Rucci, and F. Sanfilippo, Phys. Rev. D **100**, 054504 (2019).
[39] S. Borsanyi, Z. Fodor, J. N. Guenther, R. Kara, P. Parotto, A. Pasztor, L. Pirelli, and C. H. Wong, arXiv:2405.12320.
[40] S. Borsanyi, Z. Fodor, J. N. Guenther, S. D. Katz, P. Parotto, A. Pasztor, D. Pesznyak, K. K. Szabo, and C. H. Wong, Phys. Rev. D **110**, L011501 (2024).
[41] L. Adamczyk *et al.* (STAR Collaboration), Phys. Rev. C **96**, 044904 (2017).
[42] A. Andronic, P. Braun-Munzinger, K. Redlich, and J. Stachel, Nature (London) **561**, 321 (2018).
[43] C. Allton, M. Doring, S. Ejiri, S. Hands, O. Kaczmarek *et al.*, Phys. Rev. D **71**, 054508 (2005).
[44] A. Bazavov *et al.*, Phys. Rev. D **95**, 054504 (2017).
[45] S. Borsanyi, Z. Fodor, M. Giordano, J. N. Guenther, S. D. Katz, A. Pasztor, and C. H. Wong, Phys. Rev. D **107**, L091503 (2023).
[46] S. Borsanyi, Z. Fodor, M. Giordano, J. N. Guenther, S. D. Katz, A. Pasztor, and C. H. Wong, Phys. Rev. D **109**, 054509 (2024).
[47] A. Hasenfratz and D. Toussaint, Nucl. Phys. **B371**, 539 (1992).
[48] P. Hasenfratz and F. Karsch, Phys. Lett. **125B**, 308 (1983).
[49] C. Allton, S. Ejiri, S. Hands, O. Kaczmarek, F. Karsch, E. Laermann, Ch. Schmidt, and L. Scorzato, Phys. Rev. D **66**, 074507 (2002).
[50] S. Tomov, J. Dongarra, and M. Baboulin, Parallel Comput. **36**, 232 (2010).
[51] W. Bosma, J. Cannon, and C. Playoust, J. Symb. Comput. **24**, 235 (1997).
[52] C. Brown, A. Abdelfattah, S. Tomov, and J. J. Dongarra, in *2020 IEEE High Performance Extreme Computing Conference, HPEC 2020, Waltham, MA, USA* (IEEE, New York, 2020), pp. 1–7.
[53] S. Gupta, K. Huebner, and O. Kaczmarek, Phys. Rev. D **77**, 034503 (2008).
[54] M. Cheng, N. Christ, S. Datta, J. van der Heide, C. Jung *et al.*, Phys. Rev. D **77**, 014511 (2008).
[55] O. Kaczmarek, F. Karsch, P. Petreczky, and F. Zantow, Phys. Lett. B **543**, 41 (2002).
[56] P. Petreczky and H. P. Schadler, Phys. Rev. D **92**, 094517 (2015).
[57] S. Datta, S. Gupta, and A. Lytle, Phys. Rev. D **94**, 094502 (2016).
[58] C. Bonati, M. D'Elia, M. Mariti, M. Mesiti, F. Negro, and F. Sanfilippo, Phys. Rev. D **93**, 074504 (2016).
[59] S. Borsanyi *et al.*, Nature (London) **593**, 51 (2021).
[60] D. A. Clarke, P. Dimopoulos, F. Di Renzo, J. Goswami, C. Schmidt, S. Singh, and K. Zambello, arXiv:2405.10196.
[61] G. Basar, Phys. Rev. C **110**, 015203 (2024).
[62] P. Cea, L. Cosmai, and A. Papa, Phys. Rev. D **93**, 014507 (2016).
[63] C. Bonati, M. D'Elia, M. Mariti, M. Mesiti, F. Negro, and F. Sanfilippo, Phys. Rev. D **92**, 054503 (2015).
[64] R. Bellwied, S. Borsanyi, Z. Fodor, J. Günther, S. D. Katz, C. Ratti, and K. K. Szabo, Phys. Lett. B **751**, 559 (2015).
[65] A. Bazavov *et al.*, Phys. Lett. B **795**, 15 (2019).
[66] Z. Fodor and S. Katz, J. High Energy Phys. 04 (2004) 050.
[67] M. Giordano, K. Kapas, S. D. Katz, D. Nogradi, and A. Pasztor, Phys. Rev. D **102**, 034503 (2020).
[68] M. Giordano, K. Kapas, S. D. Katz, D. Nogradi, and A. Pasztor, J. High Energy Phys. 05 (2020) 088.
[69] www.gauss-centre.eu.